

tained by the approximate solutions of BSE. The first uncertainty comes from the drawback in modeling the liquid water structure by employing the generalized gradient approximation (GGA) in the framework of DFT.^{33–43} It is known that GGA predicts an over-structured liquid water.^{40–43} Thus, a significantly elevated temperature is often adopted to generate a softer HB structure closer to the experimental measurement.^{41–43} The lack of physics in accurately describing the water structure is due to the neglected van der Waals (vdW) interactions and the spurious self-interaction error⁴⁴ in GGA functional. Specifically, by including the vdW interactions, the water population in the interstitial region between the first and second coordination shells of water molecules is increased to better match experiment.⁴³ Furthermore, by mitigating the self-interaction error through the hybrid functional, the directional HB strength between water molecules are weakened towards the experiment; as a result, the protons are less easily to be donated to neighboring water molecules.⁴³ However, the effects of this improved water structure on the theoretical XAS have not been elucidated. Secondly, in the series of computational work adopting the static COHSEX approximation for the electron-hole excitation of liquid water, a homogeneous electronic screening model was first adopted⁹ and then extended by using the Hybertsen-Louie ansatz⁴⁵ to account for the inhomogeneous screening effects from the molecular environment.¹⁰ However, some discrepancies still exist and it is not yet clear that to which extent the dynamic screening effect will affect the quasiparticle wavefunctions (QWs) as well as the computed XAS. For example, it was observed that the width of the theoretical XAS by static COHSEX is slightly narrower than the experimental data.¹⁰

In an effort to address the above issues, we adopted a systematic way to study the XAS of liquid water at ambient conditions. Specifically, we used more advanced *ab initio* modelings of molecular structures and electronic excitations. We generated liquid water trajectories from the *ab initio* molecular dynamics (AIMD)⁴⁶ simulations by employing a hierarchy of XC functionals of PBE,⁴⁷ PBE with the vdW interactions in the form of Tkatchenko and Scheffler (PBE+vdW),⁴⁸ and hybrid functional PBE0^{49,50} with the vdW interactions (PBE0+vdW). By utilizing the enhanced static COHSEX method to treat the excitations⁵¹, we find that the XAS computed from the snapshot generated by the PBE0+vdW functional agree well with the experiment among the three XC functionals studied. The vdW interactions soften the water structures by increasing the population of water molecules in the interstitial region, while the hybrid functional mitigates the self-interaction error and weakens the HB strength towards experiment.⁴³ Both structural corrections and improved excitation theory are crucial in giving rise to an overall improvement of the three edges of XAS. In particular, the post-edge feature in the high-energy region of XAS is in slightly better agreement with experiment by a better screening

modeling as the enhanced static COHSEX. In addition, we also compared a set of XAS computed from different excitation theories to the experiment in order to show the importance of self-consistently diagonalized QWs in capturing the qualitative features of XAS.

II. METHODS

We performed AIMD simulations to generate liquid water trajectories using a modified version of the Quantum ESPRESSO package.⁵² We simulated 128 water molecules in a periodic cubic cell with a cell length of 15.68 Å using the Car-Parrinello molecular dynamics (CPMD)⁴⁶ within the canonical (NVT) ensemble. We employed the norm-conserving pseudopotentials in the form of Troullier-Martins⁵³ and set the kinetic energy cutoff of the electronic wavefunctions as 71 Ry. We used a hierarchy of XC functionals, including PBE, PBE+vdW, and PBE0+vdW as mentioned. The hybrid functional PBE0 with a mixing of 25% exact exchange was evaluated in a linear-scaling manner by taking advantages of maximally localized Wannier functions.³² The ionic temperatures were controlled through the Nosé-Hoover chain thermostats with a chain length of 4 for each ion.^{54–56} All AIMD simulations were performed at 330 K, where an increase of 30 K has been found to mimic the nuclear quantum effect (NQE) in structural quantities such as the oxygen-oxygen radial distribution function in DFT based simulations of liquid water.⁵⁷ A time step of 4.0 a.u. and a fictitious electron mass of 300 a.u. were chosen.

We calculated the X-ray absorption cross section using the Fermi's golden rule:

$$\sigma(\omega) = 4\pi^2\alpha_0\hbar\omega \sum_f |M_{if}|^2 \delta(\omega_{if} - \omega), \quad (1)$$

where α_0 is the fine structure constant and $\hbar\omega$ is the absorbed photon energy matching the energy difference $\hbar\omega_{if} = E_f - E_i$. E_f and E_i are the eigenvalues of the final and initial states, respectively. M_{if} are the transition matrix elements between the initial state $|\phi_i\rangle$ and final state $|\phi_f\rangle$ that can be evaluated within the electric-dipole approximation as $M_{if} \sim \langle\phi_i|x|\phi_f\rangle$, averaging over the three Cartesian directions. We take the $1s$ atomic core wavefunction from DFT calculations as the initial state $|\phi_i\rangle$. For the final state $|\phi_f\rangle$, we apply a self-consistently diagonalization procedure within the enhanced static COHSEX approach⁵¹ and the details are as follows.

The final state $|\phi_f\rangle$ is obtained by utilizing the enhanced COHSEX approach, which has been implemented within the framework of CPMD⁴⁶ scheme. Specifically, the COHSEX method has been implemented in the CPMD module within the Quantum ESPRESSO package.⁵² For each set of input wave functions $|\phi_f\rangle$, we fix the ion positions and damp the wave functions of a system in a self-consistent way as explained below. Note that the formulas we describe here are only suitable for

the excitation theory we adopt and are independent of the other CPMD simulations we performed with vdW and PBE0 functionals.

First, the Lagrangian from the CP approach is

$$\mathcal{L} = \frac{\mu}{2} \sum_i \langle \dot{\psi}_i | \dot{\psi}_i \rangle + \frac{1}{2} \sum_I M_I \dot{\mathbf{R}}_I^2 - E_{tot}(\mathbf{R}, \{\psi\}) \quad (2)$$

$$+ \lambda_{ij} (\langle \psi_i | \psi_j \rangle - \delta_{ij}),$$

where ν is a fictitious mass of electrons and ψ_i is the orbital of state i . M_I is the mass for atom I that is located at \mathbf{R}_I . $E_{tot}(\mathbf{R}, \{\psi\})$ is the total energy calculated from first-principles methods. The last part is the orthogonal-constraint imposed on orbitals with the Lagrangian multiplier to be λ_{ij} . Note that the initial ion positions are fixed and only wave functions are generated. Therefore, we need to damp the wave functions towards the ground state, which is realized via the equations of motions of electrons in plane-wave basis set

$$\mu \ddot{\psi}_i = -H(\mathbf{R}, \{\psi\})\psi_i + \sum_j \lambda_{ij} \psi_j, \quad (3)$$

respectively. Here $H(\mathbf{R}, \{\psi\})$ is the Hamiltonian matrix of the system. Furthermore, the Hamiltonian part can be evaluated in real space as

$$H\psi(\mathbf{r}) = \left[-\frac{1}{2} \nabla^2(\mathbf{r}) + V_{ext}(\mathbf{r}, \mathbf{R}) + V_H(\mathbf{r}) \right] \psi(\mathbf{r}) \quad (4)$$

$$+ \int d\mathbf{r}' \Sigma(\mathbf{r}, \mathbf{r}', E) \psi(\mathbf{r}'), \quad (5)$$

where $V_{ext}(\mathbf{r}, \mathbf{R})$ is the external potential and $V_H(\mathbf{r})$ is the Hartree potential. In particular, $\Sigma(\mathbf{r}, \mathbf{r}', E)$ is the self-energy operator that is non-local in real space and depends on the self-energy E . In the static COHSEX approximation, the self-energy operator can be approximated as

$$\Sigma_{COHSEX}^{static}(\mathbf{r}, \mathbf{r}') = \Sigma_{COH}^{static}(\mathbf{r}, \mathbf{r}') + \Sigma_{SEX}^{static}(\mathbf{r}, \mathbf{r}'). \quad (6)$$

The first part is

$$\Sigma_{COH}^{static}(\mathbf{r}, \mathbf{r}') = \frac{1}{2} \delta(\mathbf{r} - \mathbf{r}') W_p(\mathbf{r}, \mathbf{r}'; E = 0) \quad (7)$$

$$= \frac{1}{2} \delta(\mathbf{r} - \mathbf{r}') (W - v), \quad (8)$$

where W_p is the Coulomb hole, W is the screened Coulomb interaction, and v is the bare Coulomb interaction. The Hybertsen-Louie ansatz⁴⁵ proposed that W generally follows the local charge density and has a form of

$$W(\mathbf{r}, \mathbf{r}'; E = 0) = \frac{1}{2} (W[\mathbf{r} - \mathbf{r}'; \rho(\mathbf{r}')] + W[\mathbf{r}' - \mathbf{r}; \rho(\mathbf{r})]), \quad (9)$$

where W can be written as

$$W[\mathbf{r}' - \mathbf{r}; \rho(\mathbf{r})] = \frac{1}{2\pi^3} \int \epsilon^{-1}[\mathbf{q}; \rho(\mathbf{r})] v(\mathbf{q}) e^{i\mathbf{q} \cdot (\mathbf{r} - \mathbf{r}')} d\mathbf{q}. \quad (10)$$

Here, we use the Bechstedt model⁵⁸ for the dielectric function

$$\epsilon[\mathbf{q}, \rho(\mathbf{r})] = 1 + \left[(\epsilon_0 - 1)^{-1} + \alpha (q/q_{TF})^2 + q^4 / \left(\frac{4}{3} k_F^2 q_{TF}^2 \right) \right]^{-1}, \quad (11)$$

where q_{TF} is the Thomas-Fermi wave vector, k_F is the Fermi wave vector, ϵ_0 is taken from experiment, and α is fixed by matching the Bechstedt model to the q^2 dependence of the Penn model.⁵⁹ Next, we can transform W to

$$W[\mathbf{r}' - \mathbf{r}; \rho(\mathbf{r})] = \frac{v(\mathbf{r} - \mathbf{r}')}{\epsilon_0} - \frac{1}{a(x_1 - x_2)|\mathbf{r}' - \mathbf{r}|} \times \left(\frac{e^{i\sqrt{x_1}|\mathbf{r}' - \mathbf{r}|}}{x_1} - \frac{e^{i\sqrt{x_2}|\mathbf{r}' - \mathbf{r}|}}{x_2} \right). \quad (12)$$

Here $x_{1,2} = (-b \pm \sqrt{b^2 - 4ac})/2a$, $a = (\frac{4}{3} k_F^2 q_{TF}^2)^{-1}$, $b = \alpha/q_{TF}^2$, and $c = \epsilon_0/(\epsilon_0 - 1)$. The second part is

$$\Sigma_{SEX}^{static}(\mathbf{r}', \mathbf{r}) = - \sum_i^{occ} \psi_i(\mathbf{r}) \psi_i^*(\mathbf{r}') W(\mathbf{r}, \mathbf{r}'; E = 0). \quad (13)$$

Numerically it has been shown that most of the error by using the static COHSEX approximation, when compared to the GW, comes from the short-wavelength part of the assumed adiabatic accumulation of the Coulomb hole W_p , namely, the COH part; while the SEX term in the static COHSEX approximation yields relatively close values to the GW calculations.⁵¹ Therefore, the enhanced static COHSEX was proposed to introduce a universal function f to approximately include the dynamics screening in the original static model into the COHSEX formula. Specifically, the enhanced static COH term can be evaluated as

$$\Sigma_{COH}^{new}(\mathbf{r}, \mathbf{r}') = \frac{\delta(\mathbf{r} - \mathbf{r}')}{2} \int W_p(q; E = 0) f(q/k_f) e^{-i\mathbf{q} \cdot \mathbf{r}} d\mathbf{q}, \quad (14)$$

where q is a plane wave and k_f is the Fermi vector. The scaling functions is

$$f(x) = \frac{1 + a_1 x + a_2 x^2 + a_3 x^3 + a_4 x^4 + a_5 x^5 + a_6 x^6}{1 + b_1 x + b_2 x^2 + b_3 x^3 + b_4 x^4 + b_5 x^5 + b_6 x^6}, \quad (15)$$

where $a_1 = 1.9085$, $a_2 = -0.542572$, $a_3 = -2.45811$, $a_4 = 3.08067$, $a_5 = -1.806$, $a_6 = 0.410031$, $b_1 = 2.01317$, $b_2 = -1.55088$, $b_3 = 1.58466$, $b_4 = 0.368325$, $b_5 = -1.68927$, and $b_6 = 0.599225$.

In the above, we described the procedures to compute XAS based on an excited water molecule in a snapshot. We then excited every water molecule in the 128-molecule supercell in order to sample the different local environment of disordered liquid water structure. In our cases, we found converged XAS after randomly exciting 64 water molecules in the snapshot. We note that in a previous

study, 10 individual and uncorrelated snapshots of 32 water molecules were chosen and only small differences were observed between these snapshots.¹⁷ Therefore, we consider one snapshot of a large cell is sufficient to yield meaningful results and take a representative snapshot from each AIMD trajectory reflecting the equilibrated structure of liquid water to compute XAS.

Due to the different local environments in liquid water of each excited oxygen atom, we adopted the core-hole energy shift of each excitation by following Ref. 60, which is a standard approach to compute the core level shifts. We used Gaussian broadening of 0.4 eV for all spectra, which has been used in previous calculated XAS of liquid water.^{9,10} The computed XAS were aligned to the onset of the pre-edge (535 eV) and then normalized to the same area of experimental data ranging from 533 to 546 eV.

To analyze the real-space locations of QWs in terms of the three edges in XAS of liquid water, we also define the one dimensional density of QW as

$$\rho_i(r) = \int \int |\psi_i(r, \theta, \phi)|^2 d\theta d\phi, \quad (16)$$

along the radial direction and the origin is taken to be the position of the excited oxygen with a core-hole. In the equation, i represents the index of conduction band with excitation energy ε_i . In order to present the different localizations of the QWs, the index i is chosen so that $\varepsilon_i \in [534.5, 535.5]$ eV for QWs representing pre-edge of XAS, $\varepsilon_i \in [537, 539]$ eV for QWs representing main-edge of XAS, and $\varepsilon_i \in [540, 542]$ eV for QWs representing post-edge of XAS.

III. RESULTS AND DISCUSSION

A. HB structure probed by pre-, main- and post-edge of XAS

The QWs can be strongly perturbed by the local liquid water structures. The pre-edge, main-edge, and post-edge of XAS are found to have distinguishable molecular signatures that relate to different spatial regions of the HB network;^{8,9,18} the pre-edge has the $4a_1$ character while the main-edge and post-edge have the b_2 character, all of which originate from the molecular excitations in the gas phase.⁸ In order to quantitatively study the spatial regions in terms of different XAS edges, we present the density distributions of QW as a function of oxygen-oxygen distance in Fig. 1. The oxygen-oxygen radial distribution function ($g_{OO}(r)$) and an excited oxygen with QW distributed within the HB network (insets) are also shown for comparison. Overall, Figs. 1(a), (b), and (c) show that the density distributions of QW become more delocalized from the pre-edge, main-edge, to post-edge.

The density distribution of QW of pre-edge illustrated in Fig. 1(a) has the highest peak at 1.7 Å and is mostly localized within 2.75 Å, the later of which is the first peak position of $g_{OO}(r)$. The inset in Fig. 1(a) shows that the

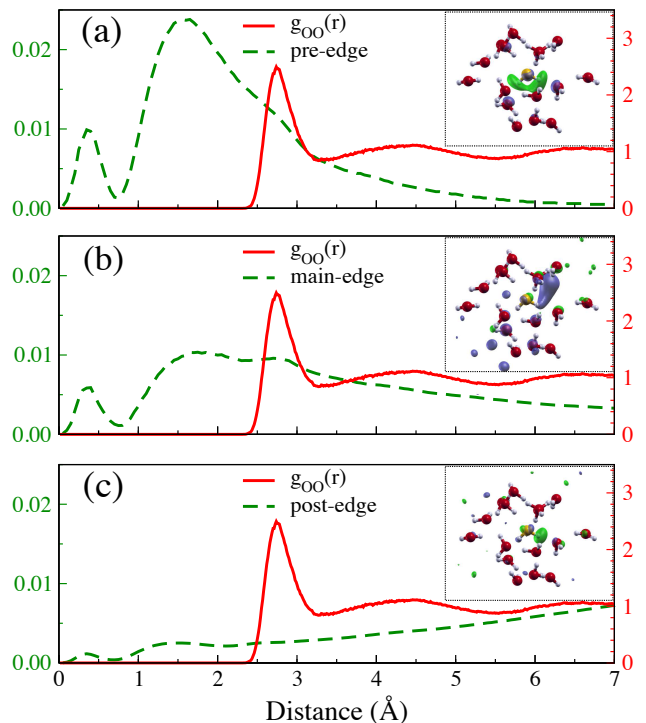


FIG. 1: Density distributions of QW (green dashed line) of (a) pre-edge, (b) main-edge, and (c) post-edge as a function of oxygen-oxygen distance computed from the snapshot of the PBE0+vdW trajectory using the enhanced static COHSEX method. The $g_{OO}(r)$ (red line) from the PBE0+vdW trajectory is shown for comparison in (a), (b), and (c). The insets show the representative QWs of the three edges around the excited water molecule. Water molecules reside within the second coordination shell of the excited oxygen are shown. Red, white, and yellow spheres represent oxygen, hydrogen, and oxygen atom with a core hole, respectively. The QWs with opposite signs are depicted with blue and green.

QW of pre-edge resembles the first excited state of water molecule in the gas phase with $4a_1$ symmetry. In this regard, our result is consistent with a previous assignment⁹ of the pre-edge to a bound exciton state, where the electron orbital was found to be mostly localized within the first coordination shell. Therefore, the pre-edge features can be largely affected by the short-range structures, such as broken HBs and covalent bond strength, around the excited oxygens. With the weakened HBs described by hybrid DFT functional (PBE0) and vdW interactions, the short-range HB network, therefore, the computed pre-edge of XAS is expected to be improved in both energies and intensities.

As shown in Fig. 1(b), the density distribution of QW of the main-edge is more delocalized than that of the pre-edge. The inset shows that the QW of main-edge can be found not only on the excited molecule itself but also on its first and second shell neighbors. In addition, a clear b_2 character can be identified for a typical QW of main-edge. The above is consistent with the fact that

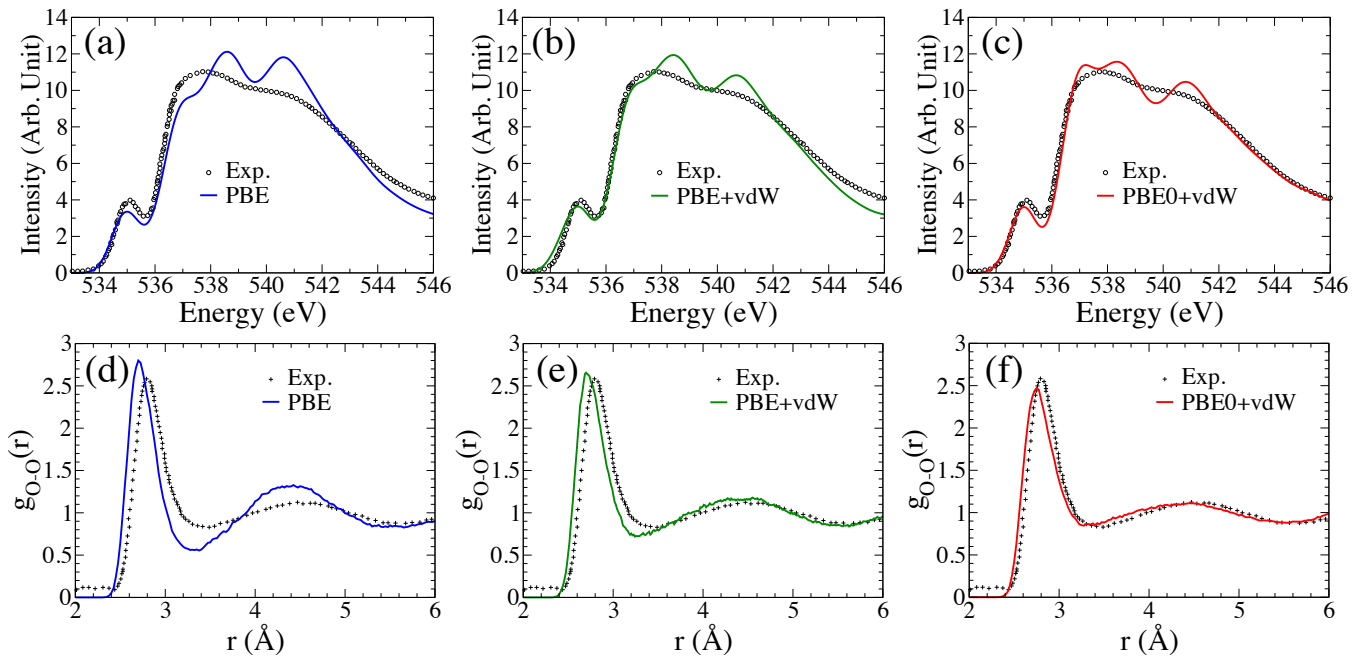


FIG. 2: Computed XAS and $g_{OO}(r)$ from three levels of exchange-correlation functionals used in the AIMD simulations, namely, PBE, PBE+vdW, and PBE0+vdW. A representative snapshot consisting of 128 water molecules from each equilibrated AIMD trajectory was used for spectra calculation. The enhanced static COHSEX method is adopted as the excitation theory. The experimental (Exp.) data of XAS²¹ and $g_{OO}(r)$ ⁶¹ are also shown for comparison.

main-edge was found to originate from the second excited state of water molecule in the gas phase. By comparing the localization of the main-edge density of QW to that of the pre-edge, it can be seen that the former one is more localized between the first and second coordination shells of liquid water structure. In this regard, it is expected that the main-edge feature of XAS will be sensitive to the intermediate-range order of liquid water structure, i.e. water molecules in the interstitial region.

In contrast to the density distributions of QW of the pre-edge and main-edge, the QW of post-edge shown in Fig. 1(c) is the most delocalized one but still preserves b_2 character. The strong delocalization can be clearly seen by the increased density of QW as a function of the distance away from the excited water molecule. Hence, the water molecules in long-range order are critical in determining the post-edge features. Using small simulation cell containing 32 water molecules fails to yield post-edge intensity of XAS in close agreement with experimental data.⁹ The delocalization feature is consistent with the fact that the post-edge is a resonant exciton state.

B. XAS calculated from PBE, PBE+vdW, and PBE0+vdW AIMD trajectories

Among the three levels of XC functionals investigated, the XAS computed from the snapshot obtained with PBE show the least agreement with the experimental spectra in Fig. 2(a). Four major discrepancies can be identified.

First, the intensity of the computed pre-edge is underestimated compared to experiment. Second, the theoretical main-edge is centered around 538.5 eV, showing a large blue-shift (around 1 eV) compared to the experimental value at 537.5 eV. Third, a significantly overestimated post-edge intensity leads to the fact that the main-edge and post-edge have almost the same intensities, which contradicts the experimental fact that the main-edge is more prominent than the post-edge in liquid water. Fourth, the width of the computed XAS is slightly narrower than the experimental XAS, especially in the high-energy region. Experimentally, the XAS of crystalline ice Ih with an intact HB network show a more prominent peak of post-edge than that of the main-edge. Therefore, the discrepancies imply that the HB network of liquid water from the PBE AIMD trajectory is over-structured. Indeed, the $g_{OO}(r)$ computed from the PBE AIMD trajectory significantly deviates from experimental measurement⁶¹ as shown in Fig. 2(d). Specifically, the first and second peaks of $g_{OO}(r)$ from simulations are significantly overestimated and the first minimum is largely underestimated. Consistently, the average number of HBs per water molecule is found to be 3.76 in the PBE trajectory according to the popular HB definition proposed by Luzar and Chandler,⁶² which is the highest among all the functionals studied herein. All the above indicate that the HB network of liquid water is over-structured from the PBE AIMD trajectory. Not surprisingly, the theoretical XAS predicted by an over-structured HB network from the PBE AIMD trajec-

tory yield ice-like spectra with relatively more prominent post-edge feature.

As shown in Fig. 2(b), the XAS computed from the PBE+vdW trajectory are largely improved towards the experimental spectra compared to that obtained from the PBE trajectory. The improvement can be seen by a higher pre-edge intensity, a shift of main-edge towards lower energy, and a lower post-edge intensity. The better agreement is attributed to the improved description of the HB network by including the vdW interactions in the AIMD simulation. An explicit account of vdW forces strengthens the attractive interactions among water molecules, which significantly increase the population of water molecules in the interstitial region. The increased population of water molecules brings the $g_{OO}(r)$ in closer agreement with experiment within the first and second coordination shells. Moreover, the increased population of water molecules in the interstitial region weakens the HBs among the water molecules in the first coordination shell, resulting in a reduced first peak in the $g_{OO}(r)$. The average number of HBs per molecule is found to be 3.56, which is about 5% smaller than that of PBE. Hence, an excited oxygen atom experiences a more disordered environment by surrounding water molecules. First of all, the pre-edge intensity is increased due to the breaking of more HBs. In order to verify this, we selected two excited water molecules, one with broken HBs and the other one with four intact HBs, and plotted their density distributions of QW in Fig. 3(a). The QW of pre-edge from the excited molecule with broken HBs is more localized with enhanced p character due to the more disordered short-range molecular environment. Therefore, larger amplitudes of transition matrices M_{ij} are obtained according to the Fermi's golden rule as shown in Eq. (1). As a result, the pre-edge intensity is increased with more broken HBs. Secondly, the main-edge intensity is also enhanced by increased population of water molecules in the interstitial region due to vdW interactions. In order to further explain how the water molecules in the interstitial region affect the main-edge features, we also selected two representative excited water molecules and calculated their density distributions of QW; one of the excited water molecules has four intact HBs and the other one has extra neighboring water molecules within the interstitial region in addition to the four intact HBs. Fig. 3(b) suggests that the density of the main-edge QW of the excited molecule with extra neighboring water molecules within the interstitial region is more localized than the other by the disordered molecular environment in the intermediate range. Similar to the discussion of the amplitudes of transition matrices and the QW localization associated with the pre-edge feature, we conclude that the increased population of water molecules within the interstitial region leads to larger amplitudes of transition matrices in the main-edge. The above discussion explains the improved main-edge features, namely, the increased intensity and shift of the peak position (centering at 538.2 eV) towards experiments (centering at

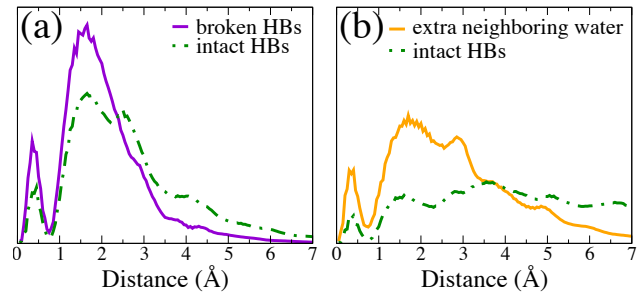


FIG. 3: Density distributions of QW computed from different excited water molecules within a snapshot of 128 water molecules for the (a) pre-edge and (b) main-edge regions of XAS. The QWs are chosen based on different H-bonding environments and different electronic states. In panel (a), density distributions of QW are shown for two water molecules with an intact HBs (green dashed line) and broken HBs (purple solid line), respectively. Note the the intact HBs refer to two accepting and two donating HBs, and prominent peaks are observed for water molecules with broken HBs as shown in (a). In panel (b), density distributions of QW are shown for two water molecules with intact HBs. In particular, the presence of an extra non-bonded neighboring water molecules within the interstitial region (orange solid line) results in more prominent peaks as shown in (b).

537.5 eV). The post-edge feature, whose QW is orthogonal to that of main-edge, is therefore predicted to have a lower spectra intensity.

The theoretical XAS are further improved towards the experimental measurements by using the molecular configurations generated from the PBE0+vdW AIMD trajectory, as shown in Fig. 2(c). By mixing a fraction of exact exchange in the hybrid functional, PBE0 mitigates the self-interaction error and lowers the tendency of hydrogens to be donated to neighboring water molecules. Under the influence of exact exchange, the covalent bonds of water molecules are strengthened, resulting in a shorter OH bond with the weakened directional HBs. Consequently, the average number of HBs is reduced to 3.48 in the PBE0+vdW AIMD trajectory, which is lower than the ones from the PBE and PBE+vdW AIMD trajectories. As a result, the water structure is further softened with a larger fraction of broken HBs, in consistence with the lower of the first peak of $g_{OO}(r)$ as illustrated in Fig. 2(f). Moreover, the width of the first peak in $g_{OO}(r)$ is broadened, and the position is slightly increased towards the experimental direction, in consistence with the weakened directional HB strength. The revised HB network in liquid water essentially affects the computed XAS in the following three aspects. First, the mitigated self-interaction error included in the hybrid functional revises the short-range order of the HB network in such a way that the excited water molecules experience a more disordered molecular environment comprising its first coordination shell, which is sensitively probed by the XAS technique in the pre-edge region. Based on

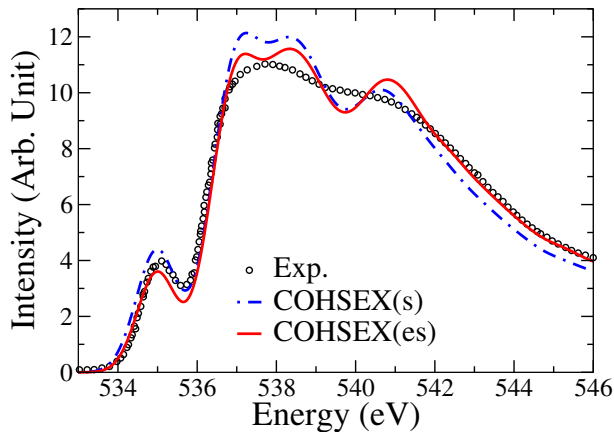


FIG. 4: Comparison of XAS computed between static COHSEX (COHSEX(s)), enhanced static COHSEX (COHSEX(es)), and the experimental data.²¹ A representative snapshot from the PBE0+vdW AIMD trajectory containing 128 water molecules was used for all spectra calculations. Self-consistent calculations were carried out to update the input wave functions.

the same argument in the previous paragraph, the QW of pre-edge with broken HBs is more localized with enhanced p character, resulting in the more prominent pre-edge intensity with more broken HBs. Therefore, the intensity of pre-edge from the PBE0+vdW trajectory is slightly increased towards the experimental spectra, reflecting the softer liquid structure at short range. Second, as a direct consequence of the weakened directional HB strength, more non-bonded water molecules flow into the interstitial region as shown by the increased first minimum towards the experimental measure in Fig. 2(f). As a result, the intermediate-range order of HB network is revised as well, in which the excited water molecule is placed in a more disordered molecular environment beyond the first coordination shell. Similar to the previous discussion of the effect of vdW interactions on main-edge, the main-edge features of XAS, which are sensitive to the intermediate-range order of the HB network, are modified with increased intensity ranging from 537 to 538 eV. In addition, the peak position of main-edge is shifted to 537.9 eV, which is closer to the experimental peak at 537.5 eV. The changes of the main-edge features provide better agreement with experimental spectra. Third, the post-edge becomes more delocalized with a decreased intensity shifting towards higher energies. The peak position of the post-edge is 540.8 eV, which is slightly smaller than the experimental value of 541.0 eV. The more prominent feature of the main-edge than that of the post-edge is best captured from the PBE0+vdW trajectory. In particular, the width of XAS is broadened in the high-energy region (544 to 546 eV), matching better with experiments.

C. Enhanced Static COHSEX and Self-Consistently Diagonalized QWs

Besides the accurate description of water structures by including the vdW interactions and hybrid functional (PBE0), a proper treatment of excitations is also critical in obtaining accurate XAS. The approximation of the electron self-energy has been widely used in the electron excitation problems, but is computationally very expensive in simulating XAS of liquid water. In order to reduce the computational cost, excitation theories based on the COHSEX method with electron screening models were used.^{9,10} Compared to the GW methods, the static COHSEX method suffers from the wavelength dependent error from the COH part, which is more significant at short wavelength but negligible at long wavelength.⁵¹ As a result, the high-energy region of XAS is affected but can be improved by using the enhanced static COHSEX method.⁵¹

Fig. 4 shows the XAS of liquid water computed by using both static COHSEX and enhanced static COHSEX methods, and the water structure is chosen from the PBE0+vdW trajectory. By using the enhanced static COHSEX method, the XAS of liquid water are improved towards experiment when compared to the spectra calculated from the static COHSEX. For example, the intensity of the post-edge region (> 541 eV) increases while intensities of the pre-edge and main-edge decrease, as obtained from the enhanced static COHSEX. This is due to the broadening effect introduced by considering the dynamic screening in the enhanced static COHSEX approach. The above broadening effect is more significant on the short-wavelength part, as can be seen by the corrections on the XAS in relatively high excitation energy region. By normalizing the XAS of both experiment and theory to the same area, the increase of the high-energy spectra also leads to the decrease of the pre-edge and main-edge intensities.

In order to emphasize the importance of self-consistently diagonalized QWs, we further compare XAS as obtained from three different excitation treatments. First, the full core-hole (FCH) approximation, where both the energy levels and wavefunctions are from unoccupied Kohn-Sham eigenstates. Second, a perturbative treatment based on the G_0W_0 approximation, in which the quasiparticle energies are from the excitation theory but the QWs are still approximated by the Kohn-Sham eigen functions. Third, the current enhanced static COHSEX approach in which both the excitation energies and the QWs are generated by the self-consistently diagonalized self-energy operator. The resulting spectra yielded from the above three different approaches are reported in Fig. 5. The G_0W_0 approximation has been widely used in calculating the band structures of water,⁶³ aqueous solutions,⁶⁴ and many other organic systems.⁶⁵⁻⁷⁰ However, calculations of the XAS significantly depend on the QWs as they are explicitly involved in the evaluation of the transition matrix elements M_{ij} in Eq. (1). Not

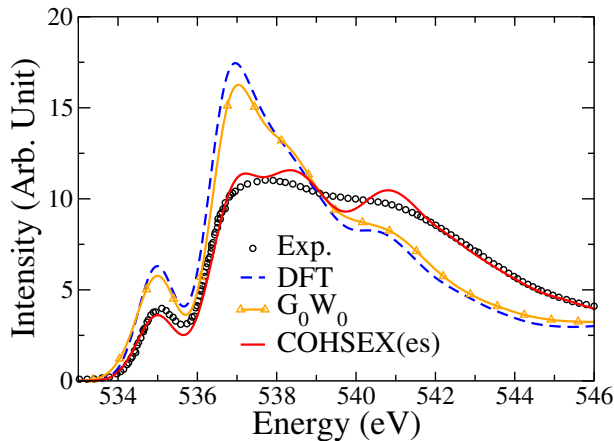


FIG. 5: Comparison of XAS computed from three different excitation schemes and the experiment.²¹ A representative snapshot from the PBE0+vdW AIMD trajectory containing 128 water molecules was used for all spectra calculations. The first excitation scheme by GGA-level DFT (blue dashed) with the FCH approximation is a one-step calculation without changing the input wave functions. Second, the G_0W_0 (orange) scheme was also performed with one-step diagonalization. Third, the enhanced static COHSEX (COHSEX(es)) (red solid line) was adopted and a self-consistent calculation was carried out to update the input wave functions.

surprisingly, the use of the wavefunctions from the FCH approximation in DFT and G_0W_0 approach leads to very similar predicted XAS. As a result, XAS from both FCH and G_0W_0 approach yield a narrowed spectra width with spectra features significantly deviating from experiments as shown in Fig. 5. In sharp contrast, XAS from self-consistently diagonalized self-energy operator within the enhanced static COHSEX approach are in much better agreement with the experimental spectra.

IV. SUMMARY

We report a systematic modeling of the liquid water XAS by advanced *ab initio* approaches. We find that the computed XAS agree better with the experiment spectra based on the liquid structure generated from AIMD by including the vdW interactions and hybrid functional

(PBE0). The predicted XAS are further improved by the enhanced static COHSEX method that includes the approximate dynamic screening. Specifically, the features of the three edges (pre-edge, main-edge, and post-edge) of liquid water are improved. First, the short-range order in liquid water is improved by inclusion of the vdW interactions and PBE0 functional. The vdW interactions increase the population of water molecules within the interstitial region and therefore weaken the short-range HBs. Under the influence of exact exchange by PBE0, the covalent OH bonds are shorter, which further weakens the directional HB strength. As a result, the pre-edge intensity is increased by the presence of more broken HBs in liquid water. An accurate description of the intermediate-range order of water, especially the water molecules in the interstitial region, is crucial to yield the main-edge intensity and peak position close to experiment. The inclusion of both vdW interactions and hybrid functional increases the population of water molecules in the interstitial region, resulting in main-edge features that agree well with the experimental spectra. Lastly, the overall spectra are improved by considering the dynamic screening effects in the enhanced static COHSEX. In conclusion, the PBE0+vdW AIMD trajectory with the enhanced static COHSEX yields better theoretical XAS. QWs from the diagonalization of the GW self-energy instead of the DFT wavefunctions are crucial in obtaining spectra that quantitatively agree with experiments.

V. ACKNOWLEDGEMENT

The authors thank Roberto Car and Giulia Galli for helpful discussions. This work was mainly supported by National Science Foundation (NSF), DMR under Award DMR-1552287 (design of the project). M.C. and M.L.K were supported by U.S. Department of Energy Scidac under Grant No. DE-SC0008726 (hybrid functional and van der Waals AIMD algorithms). This research used computational resources of the National Energy Research Scientific Computing Center (NERSC), a DOE Office of Science User Facility supported by the Office of Science of the U.S. Department of Energy under Contract No. DE-AC02-05CH11231. To whom correspondence should be addressed: xifanwu@temple.edu.

* *Corresponding author. Email: xifanwu@temple.edu

¹ P. Ball, Chem. Rev. **108**, 74 (2008).

² P. Gallo, K. Amann-Winkel, C. A. Angell, M. A. Anisimov, F. Caupin, C. Chakravarty, E. Lascaris, T. Loerting, A. Z. Panagiotopoulos, J. Russo, et al., Chem. Rev. **116**, 7463 (2016).

³ Z. Sun, G. Sun, Y. Chen, and L. Xu, Sci. China Phys. Mech. **57**, 810 (2014).

⁴ J. C. Palmer, F. Martelli, Y. Liu, R. Car, A. Z. Panagiotopoulos, and P. G. Debenedetti, Nature **510**, 385

(2014).

⁵ A. Nilsson and L. G. Pettersson, Chem. Phys. **389**, 1 (2011).

⁶ M. Leetmaa, M. Ljungberg, A. Lyubartsev, A. Nilsson, and L. G. Pettersson, J. Electron Spectrosc. Relat. Phenom. **177**, 135 (2010).

⁷ C. W. Swartz and X. Wu, Phys. Rev. Lett. **111**, 087801 (2013).

⁸ P. Wernet, D. Nordlund, U. Bergmann, M. Cavalleri, M. Odelius, H. Ogasawara, L. Å. Näslund, T. K. Hirsch,

- L. Ojamäe, P. Glatzel, et al., *Science* **304**, 995 (2004).
- ⁹ W. Chen, X. Wu, and R. Car, *Phys. Rev. Lett.* **105**, 017802 (2010).
 - ¹⁰ L. Kong, X. Wu, and R. Car, *Phys. Rev. B* **86**, 134203 (2012).
 - ¹¹ S. T. John, D. M. Shaw, D. D. Klug, S. Patchkovskii, G. Vankó, G. Monaco, and M. Krisch, *Phys. Rev. Lett.* **100**, 095502 (2008).
 - ¹² T. Head-Gordon and M. E. Johnson, *Proc. Nat. Acad. Sci.* **103**, 7973 (2006).
 - ¹³ J. D. Smith, C. D. Cappa, B. M. Messer, W. S. Drisdell, R. C. Cohen, and R. J. Saykally, *J. Phys. Chem. B* **110**, 20038 (2006).
 - ¹⁴ D. Nordlund, H. Ogasawara, K. Andersson, M. Tatarkhanov, M. Salmerón, L. Pettersson, and A. Nilsson, *Phys. Rev. B* **80**, 233404 (2009).
 - ¹⁵ J. Vinson, J. Kas, F. Vila, J. J. Rehr, and E. Shirley, *Phys. Rev. B* **85**, 045101 (2012).
 - ¹⁶ O. Fuchs, M. Zharnikov, L. Weinhardt, M. Blum, M. Weigand, Y. Zubavichus, M. Bär, F. Maier, J. D. Denlinger, C. Heske, et al., *Phys. Rev. Lett.* **100**, 027801 (2008).
 - ¹⁷ D. Prendergast and G. Galli, *Phys. Rev. Lett.* **96**, 215502 (2006).
 - ¹⁸ A. Nilsson, D. Nordlund, I. Waluyo, N. Huang, H. Ogasawara, S. Kaya, U. Bergmann, L.-Å. Näslund, H. Öström, P. Wernet, et al., *J. Electron Spectrosc. Relat. Phenom.* **177**, 99 (2010).
 - ¹⁹ T. Fransson, I. Zhovtobriukh, S. Coriani, K. T. Wikfeldt, P. Norman, and L. G. Pettersson, *Phys. Chem. Chem. Phys.* **18**, 566 (2016).
 - ²⁰ J. A. Sellberg, S. Kaya, V. H. Segtnan, C. Chen, T. Tylliszczak, H. Ogasawara, D. Nordlund, L. G. Pettersson, and A. Nilsson, *J. Chem. Phys.* **141**, 034507 (2014).
 - ²¹ S. Schreck and P. Wernet, *The Journal of Chemical Physics* **145**, 104502 (2016).
 - ²² M. Nagasaka, H. Yuzawa, T. Horigome, and N. Kosugi, *Journal of Electron Spectroscopy and Related Phenomena* (2017).
 - ²³ T. Pyllkkanen, V. M. Giordano, J.-C. Chervin, A. Sakko, M. Hakala, J. A. Soininen, K. Hamalainen, G. Monaco, and S. Huotari, *J. Phys. Chem. B* **114**, 3804 (2010).
 - ²⁴ C. J. Sahle, C. Sternemann, C. Schmidt, S. Lehtola, S. Jahn, L. Simonelli, S. Huotari, M. Hakala, T. Pyllkänen, A. Nyrow, et al., *Proc. Natl. Acad. U.S.A.* **110**, 6301 (2013).
 - ²⁵ B. Hetényi, F. De Angelis, P. Giannozzi, and R. Car, *J. Chem. Phys.* **120**, 8632 (2004).
 - ²⁶ M. Cavalleri, M. Odelius, A. Nilsson, and L. G. Pettersson, *J. Chem. Phys.* **121**, 10065 (2004).
 - ²⁷ P. Hohenberg and W. Kohn, *Phys. Rev.* **136**, 864B (1964).
 - ²⁸ W. Kohn and L. J. Sham, *Phys. Rev.* **140**, 1133A (1965).
 - ²⁹ J. Rehr, J. Soininen, and E. L. Shirley, *Physica Scripta* **2005**, 207 (2005).
 - ³⁰ J. Vinson, J. Rehr, J. Kas, and E. Shirley, *Physical Review B* **83**, 115106 (2011).
 - ³¹ G. Onida, L. Reining, and A. Rubio, *Rev. Mod. Phys.* **74**, 601 (2002).
 - ³² X. Wu, A. Selloni, and R. Car, *Phys. Rev. B* **79**, 085102 (2009).
 - ³³ D. Asthagiri, L. R. Pratt, and J. Kress, *Physical Review E* **68**, 041505 (2003).
 - ³⁴ J. C. Grossman, E. Schwegler, E. W. Draeger, F. Gygi, and G. Galli, *The Journal of chemical physics* **120**, 300 (2004).
 - ³⁵ E. Schwegler, J. C. Grossman, F. Gygi, and G. Galli, *The Journal of chemical physics* **121**, 5400 (2004).
 - ³⁶ J. VandeVondele, F. Mohamed, M. Krack, J. Hutter, M. Sprik, and M. Parrinello, *The Journal of chemical physics* **122**, 014515 (2005).
 - ³⁷ S. Yoo and S. S. Xantheas, *Communication: The effect of dispersion corrections on the melting temperature of liquid water* (2011).
 - ³⁸ A. Møgelhøj, A. K. Kelkkanen, K. T. Wikfeldt, J. Schiøtz, J. J. Mortensen, L. G. Pettersson, B. I. Lundqvist, K. W. Jacobsen, A. Nilsson, and J. K. Nørskov, *The Journal of Physical Chemistry B* **115**, 14149 (2011).
 - ³⁹ J. Wang, G. Román-Pérez, J. M. Soler, E. Artacho, and M.-V. Fernández-Serra, *The Journal of chemical physics* **134**, 024516 (2011).
 - ⁴⁰ S. Yoo, X. C. Zeng, and S. S. Xantheas, *On the phase diagram of water with density functional theory potentials: the melting temperature of ice $i h$ with the perdew-burke-ernzerhof and becke-lee-yang-parr functionals* (2009).
 - ⁴¹ C. Zhang, D. Donadio, F. Gygi, and G. Galli, *Journal of chemical theory and computation* **7**, 1443 (2011).
 - ⁴² C. Zhang, J. Wu, G. Galli, and F. Gygi, *Journal of chemical theory and computation* **7**, 3054 (2011).
 - ⁴³ R. A. DiStasio Jr, B. Santra, Z. Li, X. Wu, and R. Car, *J. Chem. Phys.* **141**, 084502 (2014).
 - ⁴⁴ J. P. Perdew and A. Zunger, *Phys. Rev. B* **23**, 5048 (1981).
 - ⁴⁵ M. S. Hybertsen and S. G. Louie, *Phys. Rev. B* **37**, 2733 (1988).
 - ⁴⁶ R. Car and M. Parrinello, *Phys. Rev. Lett.* **55**, 2471 (1985).
 - ⁴⁷ J. P. Perdew, K. Burke, and M. Ernzerhof, *Phys. Rev. Lett.* **77**, 3865 (1996).
 - ⁴⁸ A. Tkatchenko and M. Scheffler, *Phys. Rev. Lett.* **102**, 073005 (2009).
 - ⁴⁹ J. P. Perdew, M. Ernzerhof, and K. Burke, *J. Chem. Phys.* **105**, 9982 (1996).
 - ⁵⁰ C. Adamo and V. Barone, *J. Chem. Phys.* **110**, 6158 (1999).
 - ⁵¹ W. Kang and M. S. Hybertsen, *Phys. Rev. B* **82**, 195108 (2010).
 - ⁵² P. Giannozzi, S. Baroni, N. Bonini, M. Calandra, R. Car, C. Cavazzoni, D. Ceresoli, G. L. Chiarotti, M. Cococcioni, I. Dabo, et al., *J. Phys.: Condens. Matter* **21**, 395502 (2009).
 - ⁵³ N. Troullier and J. L. Martins, *Phys. Rev. B* **43**, 1993 (1991).
 - ⁵⁴ S. Nosé, *J. Chem. Phys.* **81**, 511 (1984).
 - ⁵⁵ W. G. Hoover, *Phys. Rev. A* **31**, 1695 (1985).
 - ⁵⁶ G. J. Martyna, M. L. Klein, and M. Tuckerman, *J. Chem. Phys.* **97**, 2635 (1992).
 - ⁵⁷ J. A. Morrone and R. Car, *Phys. Rev. Lett.* **101**, 017801 (2008).
 - ⁵⁸ F. Bechstedt, R. Del Sole, G. Cappellini, and L. Reining, *Solid state Commun.* **84**, 765 (1992).
 - ⁵⁹ D. R. Penn, *Phys. Rev.* **128**, 2093 (1962).
 - ⁶⁰ E. Pehlke and M. Scheffler, *Phys. Rev. Lett.* **71**, 2338 (1993).
 - ⁶¹ L. B. Skinner, C. Huang, D. Schlessinger, L. G. Pettersson, A. Nilsson, and C. J. Benmore, *J. Chem. Phys.* **138**, 074506 (2013).
 - ⁶² A. Luzar and D. Chandler, *Phys. Rev. Lett.* **76**, 928 (1996).
 - ⁶³ T. A. Pham, C. Zhang, E. Schwegler, and G. Galli, *Phys. Rev. B* **89**, 060202 (2014).
 - ⁶⁴ D. Opalka, T. A. Pham, M. Sprik, and G. Galli, *J. Chem.*

- Phys. **141**, 034501 (2014).
- ⁶⁵ X. Blase, C. Attaccalite, and V. Olevano, Phys. Rev. B **83**, 115103 (2011).
- ⁶⁶ N. Marom, F. Caruso, X. Ren, O. T. Hofmann, T. Körzdörfer, J. R. Chelikowsky, A. Rubio, M. Scheffler, and P. Rinke, Phys. Rev. B **86**, 245127 (2012).
- ⁶⁷ A. Droghetti, M. Cinchetti, and S. Sanvito, Phys. Rev. B **89**, 245137 (2014).
- ⁶⁸ T. Körzdörfer and N. Marom, Phys. Rev. B **86**, 041110 (2012).
- ⁶⁹ J. W. Knight, X. Wang, L. Gallandi, O. Dolgounitcheva, X. Ren, J. V. Ortiz, P. Rinke, T. Körzdörfer, and N. Marom, J. Chem. Theory Comput. **12**, 615 (2016).
- ⁷⁰ M. J. van Setten, F. Caruso, S. Sharifzadeh, X. Ren, M. Scheffler, F. Liu, J. Lischner, L. Lin, J. R. Deslippe, S. G. Louie, et al., J. Chem. Theory Comput. **11**, 5665 (2015).